Catalysis Today 159 (2011) 29–36

Contents lists available at ScienceDirect

Catalysis Today

journal homepage: www.elsevier.com/locate/cattod

# Catalyst design based on microkinetic models: Oxidative coupling of methane

Joris W. Thybaut[a,*], Jianjun Sun[a,1], Louis Olivier[b], André C. Van Veen[b,2], Claude Mirodatos[b], Guy B. Marin[a]

[a] Laboratory for Chemical Technology, Ghent University, Krijgslaan 281 – S5, 9000 Ghent, Belgium
[b] Institut de Recherches sur la Catalyse et l'Environnement de Lyon, CNRS, Avenue Albert Einstein 2, 69626 Villeurbanne Cedex, France

ARTICLE INFO

*Article history:*
Available online 6 October 2010

*Keywords:*
Methane oxidative coupling
Microkinetic model
Catalyst descriptor
Catalyst design
Simulation

ABSTRACT

An extended microkinetic model for methane oxidative coupling (OCM) including so-called catalyst descriptors has been used for the simulation of experimental data on various catalysts in different setups. The good agreement between experimental data and calculated results over a large range of operating conditions proves the capability of the model being incorporated in a high throughput workflow for OCM catalyst development. The model allows the selection of the optimal operating conditions for catalyst evaluation. The effects of operating conditions and catalyst texture properties such as feed flow rate, temperature, pressure and porosity, BET-surface area, and tortuosity, have been investigated using the model. By varying the value of catalyst descriptors, $C_2$ product yields have been calculated to show the effects of these descriptors on the catalytic chemistry. With this microkinetic model the yield of methane oxidative coupling products was optimized using a genetic algorithm followed by the Rosenbrock and the Levenberg–Marquardt method. The optimized parameters include catalyst descriptors, operating conditions and catalyst texture properties. Results show that even with optimal surface chemistry and operating conditions, limits exist on the attainable yield. Nevertheless, these limits were found to be beyond the yields obtained with state of the art OCM catalysts, which opens up perspectives for further catalyst improvement.



## 1. Introduction

The oxidative coupling of methane (OCM) to $C_2$ and higher hydrocarbons has been seen as a promising way to upgrade natural gas since the work of Keller and Bhasin [1] and continues to attract both industrial as well as academic interest. OCM proceeds efficiently at temperatures above 900 K with ethylene as desired product. The overall reaction, accounting for microscopic reversibility, $2CH_4 + O_2 \leftrightarrow C_2H_4 + 2H_2O$, has been found to occur through a reaction network involving homogeneous as well as heterogeneous reaction steps [2–5]. Methane interacts with oxygen species in the gas phase as well as on the catalyst surface. The latter are generated by dissociative chemisorption of oxygen and produce methyl radicals by hydrogen abstraction of methane. The radicals desorb from the catalyst surface and can couple in the gas phase to form ethane, that, in turn, can be dehydrogenated into ethylene [6–8]. The undesired deep oxidation of methyl radicals, ethane and ethylene leading to CO and $CO_2$ also occurs in gas phase as well as on the catalyst surface [2,7].

Various metal oxides have been proven to be effective OCM catalysts [2,9], but none has reached the stage of commercial application yet. A variety of promoters has already been tested to improve the performance of OCM catalysts. This unavoidably increases the size of the searching space for OCM catalysts. Fortunately, high throughput experimentation (HTE) combined with combinatorial chemistry is capable of evaluating a large number of candidate catalysts in a relatively short period of time [10]. The following aspects are included in the HTE methodology: the preparation of catalyst libraries, the screening of the catalyst properties in this library including the kinetic properties and the use of suitable software for experimental design and data treatment [11]. The catalyst optimization occurs through various catalyst generations. For each generation knowledge can be systematically extracted from the screening experiments and applied in the design of a next generation of the catalyst library [11]. Model based knowledge extraction is an important part of HTE to accelerate the development of catalyst and minimize the number of experiments required.

Boudart [12] suggested that a microkinetic analysis is the best guiding technique in the search for new or improved catalysts by combinatorial chemistry. Microkinetic analyses, as started by Dumesic et al. [13], enable incorporating the fundamental catalytic

* Corresponding author. Fax: +33 32 9 264 49 99.
*E-mail address:* Joris.Thybaut@UGent.be (J.W. Thybaut).
[1] Corus Research, Development & Technology Steelmaking, Process Metallurgy, IJmuiden Technology Centre, 4H-16 0-006, 1970 CA IJmuiden, The Netherlands.
[2] Ruhr-Universität Bochum, Bochum, D-44780, Germany.

0920-5861/$ – see front matter © 2010 Elsevier B.V. All rights reserved.
doi:10.1016/j.cattod.2010.09.002

surface chemistry into a kinetic model in the form of catalytic cycles and elementary steps. The model starts from some well-selected physical and chemical properties than can be measured independently or calculated by theoretical chemistry. The properties can be brought into relation with the unknown kinetic parameters of the elementary steps through correlations such as Polanyi's that exploit chemical similarity between various elementary steps. Understanding the subtle details of the surface chemistry and their effect on the conversion and selectivity, the catalyst composition and structure can be modified to tune the relevant rate coefficients and, hence, improve the catalyst behavior in an optimum way. Such a detailed understanding can only be obtained through microkinetic modelling which proves the benefits of such a methodology [11]. As an example, the microkinetic model of ammonia synthesis, assisted in revealing the effect of catalysts on elementary reactions at microscopic level and provided useful information for faster catalyst development [14]. Caruthers et al. [15] proposed a forward and inverse model to integrate microkinetic modelling into HTE through a so-called "knowledge extraction engine". The forward model involves two components: a catalyst chemistry model that relates the catalyst composition or descriptors of composition to the kinetic rate coefficients and a microkinetic model that is at least a qualitative, if not a quantitative representation of experiments of catalyst screening.

Another potential benefit of incorporating microkinetic models into an HTE workflow is the reliable verification of the effects of reaction conditions. As catalyst screening in HTE is generally done under unique identical conditions, there is a possibility of missing good catalysts that have better performance under different conditions [11,14]. Process parameters have been known to affect the activity and selectivity of the OCM reaction to a certain extent [9]. Featuring the consolidation of the fundamental chemical information and the reliable extrapolation of this information to other reaction conditions, a microkinetic model of OCM can help identifying the best operating conditions for the formation of the desired products, and, hence, for the use in HTE catalyst development for OCM.

Several (micro)kinetic models of OCM have been reported [16–27]. One of the first studies combining catalytic reactions and gas-phase reactions was presented by Aparicio et al. [28], followed by various other kinetic models that appended heterogeneous steps to homogeneous reaction networks [29–31]. A kinetic model developed by Couwenberg et al. [16] included the irreducible mass transport phenomena of OCM reactions. Su et al. [17] developed a model based on thermodynamic constraints, with which the effect of radical diffusion was discussed and an upper bound of $C_2$ yield of OCM, 28%, was predicted. Based on these works, Sun et al. [18] constructed a microkinetic model including so-called catalyst descriptors that can be used to study the effects of operating conditions and the catalyst texture.

In this work, we present the progress of the application of a comprehensive microkinetic model for OCM [18] in HTE with the aforementioned strategy. The effect of operating conditions and the catalyst texture is investigated with the model. Yields and selectivities exhibited by virtual methane oxidative coupling catalysts are investigated by varying the catalyst descriptor values and operating conditions. The results illustrate the effect of the catalyst descriptor values on the energetics on the catalyst surface and allow predicting a maximum yield of the desired products as a function of the catalyst descriptors and the operating conditions. Hence, the model can assist in catalyst design and development and the establishment of relationships between catalyst composition and descriptors.

**Table 1**
Catalytic elementary reactions considered in methane oxidative coupling.

| | |
|---|---|
| (1) $O_2 + 2* \rightleftharpoons 2O*$ | (10) $CHO* + O* \rightleftharpoons CO* + OH*$ |
| (2) $CH_4 + O* \rightleftharpoons CH_3\bullet + OH*$ | (11) $CO* + O* \rightleftharpoons CO_2* + *$ |
| (3) $C_2H_4 + O* \rightleftharpoons C_2H_3\bullet + OH*$ | (12) $CO + * \rightleftharpoons CO*$ |
| (4) $C_2H_6 + O* \rightleftharpoons C_2H_5\bullet + OH*$ | (13) $CO_2 + * \rightleftharpoons CO_2*$ |
| (5) $2OH* \rightleftharpoons H_2O* + O*$ | (14) $C_2H_4 + O* \rightleftharpoons C_2H_4O*$ |
| (6) $H_2O* \rightleftharpoons H_2O + *$ | (15) $C_2H_4O* + O* \rightleftharpoons C_2H_3O* + OH*$ |
| (7) $CH_3\bullet + O* \rightleftharpoons CH_3O*$ | (16) $C_2H_3O* + O* \rightleftharpoons CH_2O* + HCO*$ |
| (8) $CH_3O* + O* \rightleftharpoons CH_2O* + OH*$ | (17) $4HO_2\bullet \overset{surf}{\rightarrow} 3O_2 + 2H_2O$ |
| (9) $CH_2O* + O* \rightleftharpoons HCO* + OH*$ | |

## 2. Reaction mechanism

A more elaborate discussion of the catalytic reaction network, including a comparison with literature related mechanisms, has been given in a previous publication [18]. A summary of the most important features and reactions is given below. The microkinetic model for methane oxidative coupling is based on a reaction network that contains gas phase and catalytic reactions. This kinetic model is implemented in a one-dimensional heterogeneous reactor model, that is described in detail in the work of Couwenberg et al. [16]. Such a reactor model, making use of textural properties such as catalyst bed porosity, catalyst pellet porosity and tortuosity, allows accounting for pellet scale gradients of the reactive intermediates, even when no significant gradients for the reactants and products develop. Interactions between the catalytic elementary steps and the gas phase reactions are explicitly accounted for. The gas phase kinetics contain 39 elementary reactions among 13 molecules and 10 radicals [32]. The catalytic reaction network consists of 17 reactions, vide Table 1. It must be mentioned that while drafting the reaction network, a compromise has to be made between being as complete as possible on the one hand and having a reasonable number of adjustable parameters on the other hand, especially in the proposed methodology where microkinetics are coupled with mass transfer. In a recent publication from Sinev et al. [33] a more elaborate catalytic network was presented. The current network describes the activation of methane on the catalyst surface by the dissociation of oxygen (reaction (1)), hydrogen abstraction of methane (reaction (2)) and the regeneration of the active site (reactions (5) and (6)). It accounts for $CO_2$ generation through four reaction pathways: methyl radical scavenging followed by the sequential hydrogen abstraction from methoxy species on the catalyst (reactions (7)–(13)); hydrogen abstraction of $C_2$ surface species leading to radicals that are oxidized to $CO_2$ in the gas phase (reactions (3) and (4)); the oxidation of CO adsorbed from the gas phase (reactions (11)–(13)); and the heterogeneous oxidation of ethylene (reactions (14)–(16)). Ethylene has been recognized to be oxidized on the catalyst surface through an adsorption step followed by a single hydrogen abstraction and C–C bond cleavage. The adsorption of $CO_2$ and the hydroperoxy radical are also included to account for the inhibition effect of $CO_2$ and the quenching function of methane oxidative coupling catalyst. Especially on the nature of surface oxygen species there has been a lot of debate. Depending on the catalyst studied, surface-lattice oxygen or adsorbed oxygen species has been judged responsible for methyl radical formation [34]. On the other hand, a two-step adsorption of dioxygen followed by its dissociation [35] or a one-step dissociative adsorption of oxygen has been proposed [6], with the latter approach being followed in the present work.

### 2.1. Identification of catalyst descriptors

Catalyst descriptors correspond to a measured or calculated physical or chemical property of the catalyst in interaction with the reacting species. The catalyst descriptor can affect the reaction parameter values, such as the preexponential factor, the activation energy and the reaction enthalpy. A catalyst descriptor can be an

**Table 2**
Reaction families and corresponding parameters used in the Polanyi relationships considered in methane oxidative coupling.

| | Reaction family | $A$ | $E_0$ (kJ mol$^{-1}$) |
|---|---|---|---|
| 1 | Hydrogen abstraction by Eley–Rideal type reaction (reactions (2)–(4)) | 0.75 [5] | 144.2 |
| 2 | Hydrogen abstraction by surface reaction (reactions (8)–(10), and (15)) | 0.5 [13] | 101.5 |
| 3 | Recombination of hydroxyl (reaction (5)) | 0.65 [44] | 73.9 |
| 4 | CO oxidation on the surface (reaction (11)) | 0.26 [45] | 67.6 |
| 5 | C–C cleavage on the surface (reaction (16)) | 0.97 [45] | 185.7 |

initial sticking probability, a bond energy of a species or an atom or the density of active sites of a catalyst, etc. Incorporating one or several catalyst descriptors in a kinetic model enables the evaluation of the catalytic behavior of a catalyst family by relating the catalytic performance with its properties through the reaction kinetics. The latter ability has long been desired by catalyst researchers as a guiding tool for new catalyst development.

The identification of catalyst descriptors for methane oxidative coupling starts from a microkinetic analysis of the reaction mechanism, which is based on the catalytic cycle concept [36]. The number of catalyst descriptors depends on the extent of the reaction network and the number of independent catalytic cycles involved. Incorporation of additional reactions between already existing species in the reaction network does not increase the number of catalyst descriptors. However, if new species are involved, typically also a corresponding descriptor has to be defined. Where possible, catalyst descriptors or parameters related to the interaction between the chemical species and the catalyst are calculated through appropriate methods [17]. Otherwise this interaction parameter is taken as an adjustable parameter. Initial guesses are taken in ranges in which these descriptor values can be expected based on physic-chemical reasoning [18]. It would be desirable if catalyst descriptors could be determined by independent measurements, if they cannot be calculated. This, however, becomes realistic only when more elaborate data sets exist. This approach, although valuable, is beyond the scope of the current work.

Although the exact mechanism of the surface reactions on catalysts for methane oxidative coupling is still a matter of debate, several parallel reaction cycles have been identified on the catalyst surface such as hydrogen abstraction from $C_1$ and $C_2$ species to produce radicals and deep oxidation of methyl radicals and carbon monoxide. From the catalytic cycle describing hydrogen abstraction from methane, the corresponding reaction enthalpy is identified as a catalyst descriptor, since this elementary step involves a gas phase and a catalyst surface reactant ($CH_4$ and an oxidized site) leading towards another gas phase and catalyst surface product ($CH_3\bullet$ and the hydroxylated site). Such an elementary step is typically encountered in Eley–Rideal and Mars–Van Krevelen mechanisms. For the chemisorption of gas species on the active sites on the catalyst surface, the chemisorption enthalpy and the initial sticking probability are suitable candidate catalyst descriptors to describe differences in chemisorption strength and rates of gas phase molecule adsorption on different catalysts. For instance, the initial sticking probability of a methyl radical has been selected as a catalyst descriptor as it has a strong effect on the non-selective oxidation leading to $CO_2$ and varies with different catalysts [19]. Another property of OCM catalysts is the total concentration of active sites which, as was also seen in the kinetic modelling studies of Zanthoff et al. [29], affects decisively the calculated product yields and selectivities. Hence, it is also included in the catalyst descriptors. The selected descriptors reflect the important effects of the catalyst properties on activity and selectivity in methane oxidative coupling.

The set of catalyst descriptors in the extended microkinetic model for methane oxidative coupling, as assessed above, can be classified as follows:

(a) Reaction enthalpy of hydrogen abstraction of $CH_4$ ($D_1$).
(b) Chemisorption enthalpies of $O_2$, $CH_2O$, HCO, CO, $CO_2$, $H_2O$,$C_2H_4$ ($D_2$–$D_8$).
(c) Initial sticking probabilities of $O_2$, $CH_3\bullet$, CO, $CO_2$, $H_2O$ ($D_9$–$D_{13}$).
(d) Concentration of active sites ($D_{14}$).

### 2.2. Identification of kinetic descriptors

The above defined set of catalyst descriptors allows the calculation of the reaction enthalpies of the remaining catalytic elementary steps involved in methane oxidative coupling. Based on the reaction enthalpies, the activation energies of elementary steps are obtained by means of a Polanyi relationship for the reaction families identified in OCM (Table 2):

$$E_a = E_0 + \alpha \Delta H^0 \quad (1)$$

where $E_a$ is the activation energy of the elementary reaction. The two Polanyi parameters, i.e., $E_0$ and $\alpha$, correspond to the intrinsic activation barrier and the transfer coefficient and are the kinetic descriptors in the model.

The elementary reactions of methane oxidative coupling can be divided into 5 reaction families, each having a specific set of Polanyi parameters as shown in Table 2. As long as newly incorporated elementary reactions can be classified in one of these five families, the number of kinetic descriptors remains unchanged.

Hydrogen abstraction from methane, ethane and ethylene are considered as belonging to a single reaction family. The reaction enthalpies for hydrogen abstraction from ethane and ethylene can be obtained from catalyst descriptor $D_1$ after accounting for differences in C–H bond energy. As a result the activation energies for hydrogen abstraction of methane, ethane and ethylene can be related to each other through differences in C–H bond energy [28].

The adsorption of gas species $O_2$, $CH_3\bullet$, CO, $CO_2$, $H_2O$ is assumed to be a non-activated step. Therefore, the activation energies of the adsorption steps equal zero and the rates are determined by the corresponding catalyst descriptors, i.e., the initial sticking probabilities of the gas phase species. The activation energies of the desorption steps equal the corresponding catalyst descriptors, i.e., chemisorption enthalpies of these surface species.

The concentration of active sites of OCM catalysts can be evaluated from the transient kinetics or particle modelling [37]. The maximum concentration of $1.14 \times 10^{-5}$ mol m$^{-2}$, based on a typical area taken by a single molecule, is assumed for the concentration of active sites on the catalyst surface and fixed during the parameter estimation. Values of the same order have previously been reported in literature by other researchers, by assuming that all anion positions of the surface reveal catalytic activity [29,38].

## 3. Model formulation and computation

### 3.1. Reactor model and operating conditions

Experimental data have been acquired in two different experimental setups, one conventional setup [16,39] and a second, multi-channel reactor [10], and were used for the validation of the microkinetic model. The conventional setup was a fixed bed type

**Table 3**
Operating conditions used and catalyst properties.

| | 1 [16,39] | | 2 [10] | |
|---|---|---|---|---|
| Pressure (kPa) | 108.0–130.0 | | 101.0 | |
| Temperature (K) | 947.0–1013.0 | | 1073.0 | |
| $CH_4/O_2$ (mol mol$^{-1}$) | 2.0–12.0 | | 2.0 | |
| $W/F_{t,0}$ (kg mol$^{-1}$ s) | 2.0–12.0 | | 4.0 | |
| Diameter of catalyst pellet (m) | $2.5 \times 10^{-4}$ | | $3.0 \times 10^{-4}$ | |
| Catalyst | Sn/Li/MgO | Li/MgO | Li/MgO | La–Sr/CaO |
| BET surface area (m$^2$ kg$^{-1}$) | 2800.0 | 1000.0 | 2450 | 67,300 |
| Density (kg m$^{-3}$) 2300.0[a] | 2350.0[a] | 635.1[b] | 477.3[b] | |

[a] Pellet density.
[b] Bed bulk density.

of reactor packed with catalyst pellets under the reaction conditions listed in Table 3 [16]. The catalyst bed was diluted with inert pellets to reduce radial-temperature gradients. The reaction effluent analysis was performed using gas chromatography. The parallel screening setup consisted of a 6-channel reactor in a fixed bed configuration [10]. Products were analyzed using mass spectrometry in an automated fashion for each channel. The operating conditions and catalyst properties are also reported in Table 3.

The kinetic model has been implemented in a one-dimensional heterogeneous reactor model that was previously developed [39,40]. The latter model consists of a set of partial differential equations to calculate the concentration profiles in both the gas phase and the pores of the solid phase. Orthogonal collocation is used to transform the equations to a set of ordinary differential equations coupled with algebraic equations. The resulting simulation model is applicable over a broad range of operating conditions.

### 3.2. Parameter estimation

Parameter estimation was performed using the Rosenbrock methodology [41] for the initial minimization of the objective function followed by a Levenberg–Marquardt algorithm, i.e., ODRPACK-package version 2.01 [42] for the final optimization. The objective function used is the weighed sum of the squared residuals, between the observed, $y$, and calculated, $\hat{y}$, mole fractions at the reactor outlet.

$$S(b) = \sum_{j=1}^{nrespnresp} \sum_{k=1} \sigma_{j,k}^{-1} \sum_{i=1}^{nobs} (y_{i,j} - \hat{y}_{i,j})(y_{i,k} - \hat{y}_{i,k}) \xrightarrow{b} \min \quad (2)$$

where $b$ is the parameter vector containing the adjustable parameters; $\sigma_{j,k}^{-1}$ is an element of the inverse of the error variance–covariance matrix, which is calculated from replicate experiments or estimated from the observed and calculated molar fractions at the reactor outlet. The objective function $S$ was minimized by adjusting the model parameter vector $b$. The estimated parameters are the catalyst and kinetic descriptors as discussed in Sections 2.1 and 2.2.

### 3.3. Optimization of the OCM performance by tuning the catalyst properties and the operating conditions

The quest for the ideal combination of catalyst properties and operating conditions can be formulated as a mathematical optimization problem, provided that an appropriate objective function is defined, e.g., as a function of the $C_2$ products yield. The model that relates the catalyst descriptors and the operating conditions to $C_2$ yields and selectivities consists of a set of differential–algebraic equations which is highly non-linear in the model parameters.

$$\frac{\partial c_j}{\partial z} = g(c, z, x) \quad \text{with} \quad j = (H_2, H_2O, H_2O_2, O_2, CH_4, CH_2O, CH_3OH, C_2H_2, C_2H_4, C_2H_6, C_3H_6, C_3H_8, CH_3 \bullet \ldots)$$
$$0 = h(c, z, x)$$
$$c_j(z_0) = c_{j,0}$$
$$z \in [0, 1]$$

where $c$ is the vector of molar concentration of reactants and products in the reactor, $z$ is the coordinate of reactor. As a result, the solution of this problem is expected to produce multiple local optimums.

Given the large number of degrees of freedom and the high degree of non-linearity with respect to the adjustable parameters in this optimization, a genetic algorithm, which is a general tool for searching global optimum, was applied first. The optimum found by this algorithm was then further refined using the same methodologies as those used in parameter estimation. The latter optimization methods that rely on gradient-based search directions failed in finding the optimum point in a wide range. In this optimization problem, the allowed ranges, vide Table 4, were set in accordance with available literature data [1,11]. The parameters of the genetic algorithm were set as follows—population size: 1000, crossover rate: 0.5, mutation ratio: 0.01, and maximum generation: 300.

During the calculation, the upper and lower bound of activation energy of catalytic reactions are set as 300 kJ mol$^{-1}$ and 0 kJ mol$^{-1}$, respectively.

## 4. Results and discussion

### 4.1. Model validation

The model has in the first instance been validated against literature data on Li/MgO and a Sn promoted version of this catalyst [16,39]. Catalyst as well as kinetic descriptors have been estimated, leading to a good overall description of the data, vide Fig. 1. The final

**Table 4**
Adjustable parameters in the virtual screening and corresponding ranges set.

| | |
|---|---|
| Pressure (Pa) | $1.0 \times 10^5$–$1.6 \times 10^5$ |
| Temperature (K) | 940.0–1110.0 |
| $CH_4/O_2$ | 2.0–12.0 |
| $W/F_{t,0}$ (kg s mol$^{-1}$) | 2.0–12.0 |
| Porosity of catalyst | 0.1–0.6 |
| BET (m$^2$ kg$^{-1}$) | $1.0 \times 10^3$–$3.5 \times 10^4$ |
| Radius of catalyst pellet (m) | $1.0 \times 10^{-4}$–$1.0 \times 10^{-3}$ |
| Tortuosity of catalyst | 2.0–10.0 |
| Reaction enthalpy of hydrogen abstraction ($D_1$) | 0.0–200.0 |
| Chemisorption enthalpy of $O_2$, $CH_2O$, HCO, CO, $CO_2$, $H_2O$, $C_2H_4$ (kJ mol$^{-1}$) | 20.0–300.0 |
| Initial sticking probability of $O_2$, $CH_3\bullet$, CO, and $CO_2$ | $10^{-7}$–1.0 |

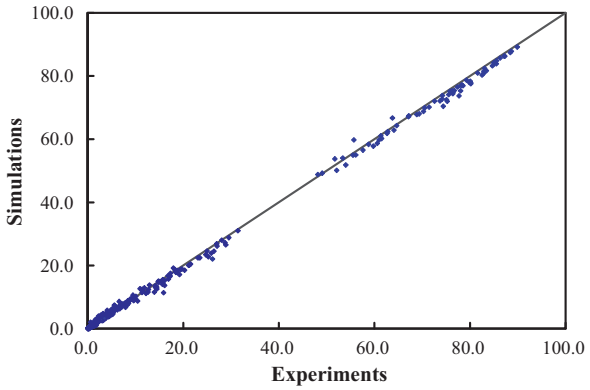


**Fig. 1.** Parity diagram for the product outlet molar percentages on Li/MgO and Sn/Li/MgO obtained using the fixed bed reactor [16,40]. The calculated molar percentages are obtained with the microkinetic model with the gas phase reactions and corresponding parameters as reported in [18] and the surface reactions as reported in Table 1. The parameters related to the surface reactions are calculated from the values reported in Table 2 for the Polanyi relationship and in Table 6 for the catalyst descriptors. The reactor model used is discussed in Section 3.1

**Table 5**
Experimental results obtained on the OCM catalysts tested in the 6-channel reactor.

| Catalyst | Li/MgO | La–Sr/CaO |
|---|---|---|
| $CH_4$ conversion | 15 | 40 |
| $O_2$ conversion | 33 | 97 |
| $C_2$ selectivity | 74 | 47 |
| $C_2$ yield | 11.1 | 18.8 |

descriptor values can be found in the work of Sun et al. [18]. The same model has been used in the assessment of new experimental data obtained in a sixfold quartz tube reactor on another Li/MgO and a La–Sr/CaO catalyst [10]. The former catalyst is less active than the latter one, vide Table 5: near full oxygen conversion is obtained on the La–Sr/CaO while conversions on the Li/MgO are limited to 15% and 33% for methane and oxygen. The combination of conversion and selectivity is such that the highest yields are obtained on the La–Sr/CaO catalyst.

In the regression of the kinetic data on each of the two new catalysts, 5 catalyst descriptors, i.e., the ones to which the simulation results were found to be the most sensitive, were allowed to vary, vide Table 6. The major differences are obtained in the water and the ethylene chemisorption enthalpies. Both components adsorb much weaker on the La–Sr/CaO catalyst than on the Li/MgO catalyst while only minor differences are observed for the hydrogen abstraction enthalpy from methane and the oxygen chemisorption enthalpy. The weaker adsorption of water on La–Sr/CaO results in a higher availability of the active sites for the other reactive species on the catalyst surface and, hence, a higher conversion. The stronger interaction of ethylene as well as the higher initial sticking probability of the methyl radical on the Li/MgO catalyst result in lower selectivities on this catalyst at equal conversion and, hence, lower $C_2$ yields. The simulation results, vide Figs. 2 and 3, show a good agreement between experimental data and simulation results.

**Table 6**
Catalyst descriptors used in the simulation of the data obtained on Li/MgO and La–Sr/CaO using the six channel parallel reactor.

| Catalyst | Li/MgO | La–Sr/CaO |
|---|---|---|
| $D_1$ (kJ mol$^{-1}$) | 58.4 | 59.0 |
| $D_2$ (kJ mol$^{-1}$) | 107.7 | 103.2 |
| $D_3$ (kJ mol$^{-1}$) | 91.7 | |
| $D_4$ (kJ mol$^{-1}$) | 233.6 | |
| $D_5$ (kJ mol$^{-1}$) | 101.4 | |
| $D_6$ (kJ mol$^{-1}$) | 160.9 | |
| $D_7$ (kJ mol$^{-1}$) | 54.2 | 39.5 |
| $D_8$ (kJ mol$^{-1}$) | 64.7 | 56.2 |
| $D_9$ | 0.4 | |
| $D_{10}$ | $3.3 \times 10^{-5}$ | $1.1 \times 10^{-5}$ |
| $D_{11}$ | 0.008 | |
| $D_{12}$ | $1.0 \times 10^{-5}$ | |
| $D_{13}$ | 0.6 | |
| $D_{14}$ (mol m$^{-2}$) | $1.14 \times 10^{-5}$ | |

Reaction enthalpy of hydrogen abstraction of $CH_4$ ($D_1$); chemisorption enthalpies of $O_2$, $CH_2O$, HCO, CO, $CO_2$, $H_2O$, $C_2H_4$ ($D_2$–$D_8$); initial sticking probabilities of $O_2$, $CH_3\bullet$, CO, $CO_2$, $H_2O$ ($D_9$–$D_{13}$); concentration of active sites ($D_{14}$).

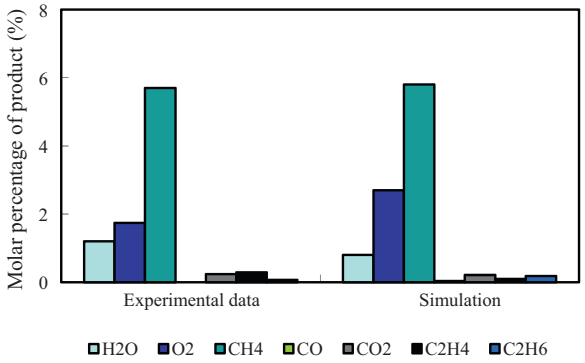


**Fig. 2.** Comparison of product distributions of Li/MgO between experiment [10] and simulation. The calculated molar percentages are obtained with the microkinetic model with the gas phase reactions and corresponding parameters as reported in [18] and the surface reactions as reported in Table 1. The parameters related to the surface reactions are calculated from the values reported in Table 2 for the Polanyi relationship and in Table 6 for the catalyst descriptors. The reactor model used is discussed in Section 3.1.

### 4.2. Operating conditions and catalyst texture effect

It is well known that the catalyst texture affects the observed reaction kinetics, but the extent of these effects is not a priori clear and may depend on the reaction conditions considered. In this section, the effects of catalyst textural properties such as porosity, BET surface area, tortuosity and catalyst pellet diameter have been studied. Such properties are expected to be of paramount importance to methane oxidative coupling since the reaction scheme involves a complex interplay between gas phase and surface elementary steps [9].

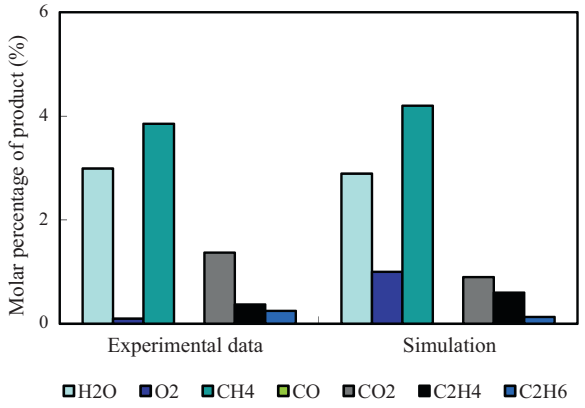


**Fig. 3.** Comparison of product distributions of La–Sr/CaO between experiment [10] and simulation. The calculated molar percentages are obtained with the microkinetic model with the gas phase reactions and corresponding parameters as reported in [18] and the surface reactions as reported in Table 1. The parameters related to the surface reactions are calculated from the values reported in Table 2 for the Polanyi relationship and in Table 6 for the catalyst descriptors. The reactor model used is discussed in Section 3.1.

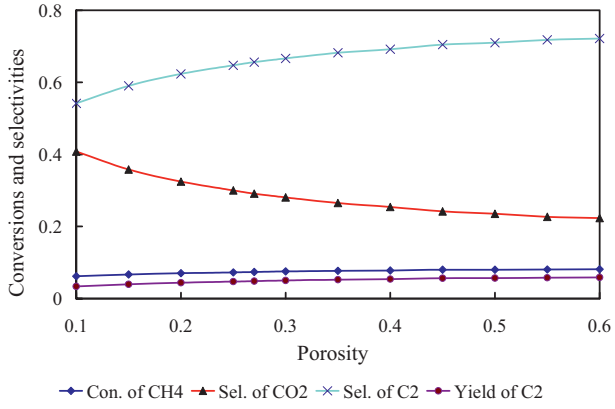


**Fig. 4.** Conversion and selectivities vs. porosity of Sn/Li/MgO. (Operating conditions: $T = 973$ K; $p = 108$ kPa; $CH_4/O_2 = 3.7$; $W/F_{t,0} = 3.9$ kg s mol$^{-1}$; BET surface area = 2800 m$^2$ kg$^{-1}$; tortuosity = 5.0; diameter of catalyst pellet = $2.5 \times 10^{-4}$ m, $O_2$ conversion: 20–30%.) The calculated conversion and selectivities are obtained with the microkinetic model with the gas phase reactions and corresponding parameters as reported in [18] and the surface reactions as reported in Table 1. The parameters related to the surface reactions are calculated from the values reported in Table 2 for the Polanyi relationship and in Table 6 for the catalyst descriptors. The reactor model used is discussed in Section 3.1.

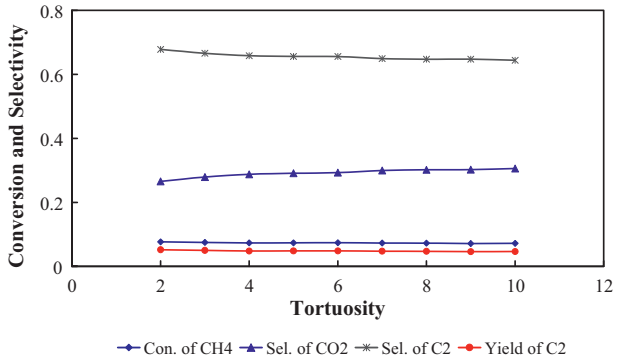


**Fig. 6.** Conversion and selectivities vs. tortuosity of Sn/Li/MgO. (Operating conditions: $T = 973$ K; $p = 108$ kPa; $CH_4/O_2 = 3.7$; $W/F_{t,0} = 3.9$ kg s mol$^{-1}$; porosity = 0.27; BET surface area = 2800 m$^2$ kg$^{-1}$; diameter of catalyst pellet = $2.5 \times 10^{-4}$ m, $O_2$ conversion: 20–30%.). The calculated conversion and selectivities are obtained with the microkinetic model with the gas phase reactions and corresponding parameters as reported in [18] and the surface reactions as reported in Table 1. The parameters related to the surface reactions are calculated from the values reported in Table 2 for the Polanyi relationship and in Table 6 for the catalyst descriptors. The reactor model used is discussed in Section 3.1.

The simulations were performed with the model parameter values as determined for Sn/Li/MgO. The experimental conditions were given in Table 3. The simulations were performed by varying the value of a texture property in a specified range while keeping the other properties constant.

Fig. 4 shows that, as the porosity increases, the conversion of methane and the selectivity towards $C_2$ products increase. Hence, the yield of $C_2$ products increases. An increased porosity means an increased gas phase contribution inside the catalyst pores, favouring the coupling of methyl radicals in the gas phase and, hence, an enhancement of $C_2$ species production.

As the BET surface area increases (Fig. 5), the selectivity towards $CO_2$ increases at the expense of the selectivity towards $C_2$ products. However, the increasing conversion of methane compensates this undesired effect in such a way that yield of $C_2$ products first increases with the BET surface before reaching a constant value from a BET surface area of 10,000 m$^2$ kg$^{-1}$ on. In the performed simulations, higher BET surface areas at a constant porosity correspond to smaller catalyst pore diameters. As a result diffusional limitations will become more important and products formed will be more likely to undergo consecutive reactions leading to lower selectivities. In addition, an increased BET surface area results in a corresponding increase of the rate of the catalytic reactions, whereas the rate of the gas phase reactions is not affected because of the constant porosity. As a result more methyl radicals are produced but also radical quenching is enhanced compared to the coupling in the gas phase. Despite the lower $C_2$ selectivities, the overall $C_2$ yield increases with the BET surface area because of the higher reaction rates.

Fig. 6 indicates that the conversion of methane and the selectivity towards $C_2$ products decrease mildly with increasing tortuosity. Hence, the yield of $C_2$ products also decreases. This decrease can be explained by the increased diffusion resistance accompanying the higher tortuosity. The mild effect of the tortuosity on the simulated conversion and selectivity indicates that, in the explanation of the BET surface area effect, the dominant factor is the change in relative importance of the gas phase and the catalytic reactions, rather than diffusional effects.

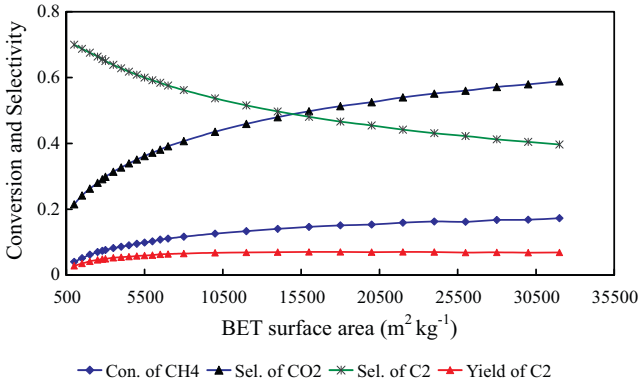


**Fig. 5.** Conversion and selectivities vs. BET surface area of Sn/Li/MgO. (Operating conditions: $T = 973$ K; $p = 108$ kPa; $CH_4/O_2 = 3.7$; $W/F_{t,0} = 3.9$ kg s mol$^{-1}$; porosity = 0.27; tortuosity = 5.0; diameter of catalyst pellet = $2.5 \times 10^{-4}$ m, $O_2$ conversion: 10–85%.). The calculated conversion and selectivities are obtained with the microkinetic model with the gas phase reactions and corresponding parameters as reported in [18] and the surface reactions as reported in Table 1. The parameters related to the surface reactions are calculated from the values reported in Table 2 for the Polanyi relationship and in Table 6 for the catalyst descriptors. The reactor model used is discussed in Section 3.1.

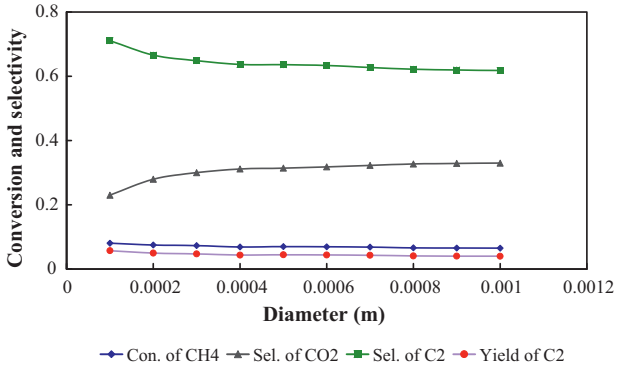


**Fig. 7.** Conversion and selectivities vs. diameter of catalyst pellet of Sn/Li/MgO. (Operating conditions: $T = 973$ K; $p = 108$ kPa; $CH_4/O_2 = 3.7$; $W/F_{t,0} = 3.9$ kg s mol$^{-1}$; porosity = 0.27; BET surface area = 2800 m$^2$ kg$^{-1}$; tortuosity = 5.0, $O_2$ conversion: 20–30%.) The calculated conversion and selectivities are obtained with the microkinetic model with the gas phase reactions and corresponding parameters as reported in [18] and the surface reactions as reported in Table 1. The parameters related to the surface reactions are calculated from the values reported in Table 2 for the Polanyi relationship and in Table 6 for the catalyst descriptors. The reactor model used is discussed in Section 3.1.

In Fig. 7, it is observed that the conversion of methane and the selectivity towards $C_2$ products decrease as the diameter of catalyst pellet is increasing. Hence, also the yield of $C_2$ products decreases. Diffusional phenomena that are most likely to occur at larger particle diameters are at the origin of the enhancement of consecutive reactions in general and total oxidation reactions in particular.

### 4.3. Virtual screening OCM catalysts at fixed operating conditions

It has been identified that the reaction enthalpy of hydrogen abstraction of methane ($D_1$) and the chemisorption enthalpy of oxygen ($D_2$) are the key parameters that determine the yield of $C_2$ components [17], i.e., small changes in the values of these model parameters can have a significant effect on the simulated conversion, yield and selectivity. The effects of these two catalyst descriptors on the $C_2$ yield have been investigated with the microkinetic model of OCM. With the experimental conditions of Sn/Li/MgO, under which the best yield of $C_2$ products has been obtained, the simulations performed by varying the values of two catalyst descriptors (Fig. 8) indicate that a 4% increase of the $C_2$ products yield can be achieved. This enhanced $C_2$ yield requires a catalyst with an increased oxygen chemisorption enthalpy and hydrogen abstraction enthalpy by about 25 kJ mol$^{-1}$. The operating conditions, however, have a tremendous effect on the maximum achievable $C_2$ yield as well as on the corresponding catalyst descriptor values.

An identical virtual OCM catalyst screening has been performed at the operating conditions at which the most advanced state of the art catalysts for methane oxidative coupling have their maximum $C_2$ yield of about 27%, i.e., at 1069 K and a $CH_4/O_2$ inlet molar ratio of 3.0 [43]. The above described microkinetic model is used to analyze which are the key catalyst properties and corresponding descriptors in order to achieve such a catalyst performance. Apart from the temperature, which is increased to 1069 K, the operating conditions used in the simulations were not changed. The initial sticking probability of $CH_3\bullet$, $D_{9,}$ was decreased from $3.3 \times 10^{-5}$ to $10^{-7}$, which is the lowest value measured for OCM catalyst [19]. The reaction enthalpy of hydrogen abstraction of methane and the chemisorption enthalpy of oxygen were varied in the range from

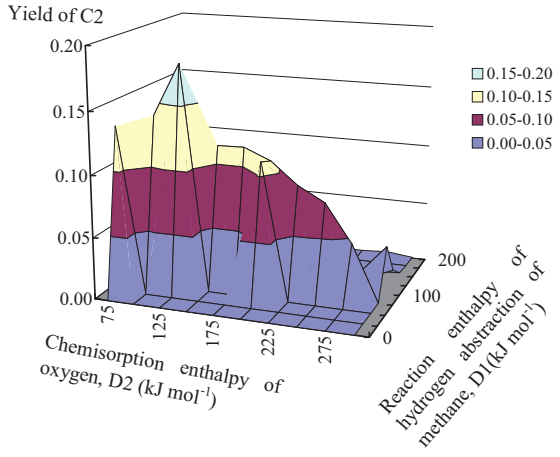


**Fig. 8.** Yield of $C_2$ products vs. catalyst descriptors $D_1$ and $D_2$. (Operating conditions: $T$ = 1012 K; $p$ = 108 kPa; $CH_4/O_2$ = 3.0; $W/F_{t,0}$ = 11.0 kg s mol$^{-1}$. The simulations were performed with the microkinetic model with the gas phase reactions and corresponding parameters as reported in [18] and the surface reactions as reported in Table 1. The parameters related to the surface reactions are calculated from the values reported in Table 2 for the Polanyi relationship and in Table 6 for the catalyst descriptors. The values of catalyst descriptor $D_1$ and $D_2$ were varied in the range from 0 to 300 kJ mol$^{-1}$ and from 0 to 200 kJ mol$^{-1}$, respectively). The reactor model used is discussed in Section 3.1.

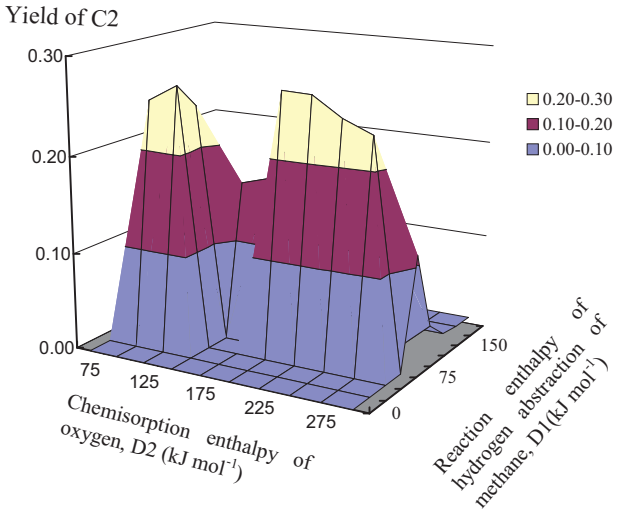


**Fig. 9.** Yield of $C_2$ products vs. catalyst descriptors $D_1$ and $D_2$ under 1069 K. (Operating conditions: $T$ = 1069 K, $p$ = 108 kPa, $CH_4/O_2$ = 3.0, $W/F_{t,0}$ = 11.0 kg s mol$^{-1}$. The simulations were performed with the microkinetic model with the gas phase reactions and corresponding parameters as reported in [18] and the surface reactions as reported in Table 1. The parameters related to the surface reactions are calculated from the values reported in Table 2 for the Polanyi relationship and in Table 6 for the catalyst descriptors. The values of catalyst descriptor $D_1$ and $D_2$ were varied in the range from 0 to 300 kJ mol$^{-1}$ and from 0 to 200 kJ mol$^{-1}$, respectively.). The reactor model used is discussed in Section 3.1.

0 to 200 kJ/mol and 0 to 300 kJ/mol. The simulation results, vide Fig. 9, indicate two maxima in the $C_2$ yield at 0.27.

### 4.4. Optimization of catalyst behavior as a function of catalyst properties and operating conditions

Of course, the yield optimization should not be limited to the variation of the 2 catalyst descriptors considered in Section 4.3. The operating conditions as well as the other catalyst properties/descriptors can also affect the yield of $C_2$ products. The final set of values leading to optimal catalyst behavior is listed in Tables 7a and 7b. A search for the optimal combination of operating conditions and catalyst descriptors results in a yield of $C_2$ products of ≈35%.

Compared to the descriptor values obtained above for the Li/MgO and the La–Sr/CaO, especially the $O_2$ chemisorption enthalpy indicates very strong bonding of $O_2$ to the surface and also the hydrogen abstraction enthalpy from $CH_4$ is somewhat more exothermic. The chemisorption enthalpies of the other components in the reaction mixture do not vary much, except for water and ethylene, which, at optimal $C_2$ yield, both interact even less strong

**Table 7a**
Values of the catalyst descriptors leading to the optimal $C_2$ yield of 35%.

| | |
|---|---|
| Reaction enthalpy of hydrogen abstraction of $CH_4$ ($D_1$) | 72.46 |
| Chemisorption enthalpy of $O_2$ ($D_2$) | 224.10 |
| Chemisorption enthalpy of $CH_2O$ ($D_3$) | 91.68 |
| Chemisorption enthalpy of HCO ($D_4$) | 234.01 |
| Chemisorption enthalpy of CO ($D_5$) | 101.42 |
| Chemisorption enthalpy of $CO_2$ ($D_6$) | 160.90 |
| Chemisorption enthalpy of $H_2O$ ($D_7$) | 38.50 |
| Chemisorption enthalpy of $C_2H_4$ ($D_8$) | 51.58 |
| Initial sticking probability of $O_2$ ($D_9$) | 0.44 |
| Initial sticking probability of $CH_3\bullet$ ($D_{10}$) | $1.0 \times 10^{-7}$ |
| Initial sticking probability of CO ($D_{11}$) | $4.0 \times 10^{-7}$ |
| Initial sticking probability of $CO_2$ ($D_{12}$) | 0.02 |
| Initial sticking probability of $H_2O$ ($D_{13}$) | $1.0 \times 10^{-5}$ |
| Total concentration of active sites ($D_{14}$) | $1.14 \times 10^{-5}$ |

Enthalpy: kJ mol$^{-1}$.

**Table 7b**
Operating conditions leading to the optimal $C_2$ yield of 35%.

| | |
|---|---|
| Pressure (Pa) | $1.1 \times 10^5$ |
| Temperature (K) | 1073.0 |
| $CH_4/O_2$ | 2.70 |
| $W/F_{t,0}$ (kg s mol$^{-1}$) | 12 |
| Porosity of catalyst | 0.39 |
| BET (m$^2$ kg$^{-1}$) | 5156.0 |
| Radius of catalyst pellet (m) | $1.0 \times 10^{-4}$ |
| Tortuosity of catalyst | 7.28 |

with the catalyst surface than on the La–Sr/CaO. The initial sticking probabilities of the methyl radical and CO are very low and correspond to a decrease of the reaction rate of undesired reactions. The initial sticking probability of $CO_2$, on the other hand, is on the high side which can be related to an enhancement of reverse reactions.

Optimal $C_2$ yields are obtained at relatively high temperatures favoring the gas phase reactions. With an inlet molar methane to oxygen ratio of 2.7, the optimal feedstock composition does not contain an excessive amount of methane compared to oxygen. The catalyst porosity, BET surface area and tortuosity are well within the range investigated in Section 4.2. It is only the catalyst pellet diameter which goes to extremely low values, corresponding to a situation with the lowest internal resistances against mass transfer and, hence, the lowest probabilities towards consecutive total oxidation reactions.

## 5. Conclusions

A microkinetic model used previously in the assessment of OCM data on a Li/MgO and a Sn promoted version of this catalyst has been successfully extended to a new Li/MgO and a La–Sr/CaO catalyst. Water as well as ethylene interaction with the catalyst surface is much weaker on La–Sr/CaO than on Li/MgO. The numerical values for the methane hydrogen abstraction reaction enthalpy and the oxygen chemisorption enthalpy vary less, but still significantly affect the model predictions. The catalyst texture determines the overall OCM behavior by affecting the relative contribution of gas phase and catalytic reactions as well as the extent of diffusion of reactive intermediates. A virtual screening of OCM catalysts varying a limited number of parameters may confirm the optimal catalyst behavior or indicate potential improvements. An optimal $C_2$ yield is obtained at higher temperatures on catalyst pellets with a very low diameter. Moreover, oxygen interaction with the catalytic surface should be strong, whereas the interaction with water and ethylene should be weak. The above analysis shows how a microkinetic model with catalyst descriptors is a useful tool in the assessment of HTE data and how it is capable of providing insight in the optimal OCM reaction system. Of course, the exploitation of this insight requires the establishment of relationships between the synthesis conditions and the catalyst descriptors.

## Acknowledgement

The study is supported by the European research project "TOPCOMBI" (contract NMP2-CT2005-515792).

## References

[1] G.E. Keller, M.M. Bhasin, Journal of Catalysis 73 (1982) 9.
[2] G.A. Martin, C. Mirodatos, Fuel Processing Technology 42 (1995) 179.
[3] J.G. McCarty, Mechanism of Cooxidative Methane Dimerization Catalysis: Kinetic and Thermodynamic Aspects, Van Nostrand Reinhold, New York, 1992.
[4] P.F. Nelson, C.A. Lukey, N.W. Cant, Journal of Physical Chemistry 92 (1988) 6176.
[5] O.V. Krylov, Catalysis Today 18 (1993) 209.
[6] R.H. Nibbelke, J. Scheerova, M.H.J.M. de Croon, G.B. Marin, Journal of Catalysis 156 (1995) 106.
[7] J.H. Lunsford, Langmuir 5 (1989) 12.
[8] E.P.J. Mallens, J.H.B.J. Hoebink, G.B. Marin, Journal of Catalysis 160 (1996) 222.
[9] Z. Zhang, X.E. Verykios, M. Baerns, Catalysis Reviews-Science and Engineering 36 (1994) 507.
[10] L. Olivier, S. Haag, H. Pennemann, C. Hofmann, C. Mirodatos, A.C.v. Veen, Catalyst Today 137 (2008) 80.
[11] W.F. Maier, K. Stowe, S. Sieg, Angewandte Chemie-International Edition 46 (2007) 6016.
[12] M. Boudart, Catalysis Letters 65 (2000) 1.
[13] J.A. Dumesic, D.F. Rudd, L.M. Aparicio, J.E. Rekoske, The Microkinetics of Heterogeneous Catalysis, American Chemical Society, Washington, DC, 1993.
[14] A.G. Hansen, W.J.M. Van Well, P. Stoltze, Topics in Catalysis 45 (2007) 219.
[15] J.M. Caruthers, J.A. Lauterbach, K.T. Thomson, V. Venkatasubramanian, C.M. Snively, A. Bhan, S. Katare, G. Oskarsdottir, Journal of Catalysis 216 (2003) 98.
[16] P.M. Couwenberg, Q. Chen, G.B. Marin, Industrial & Engineering Chemistry Research 35 (1996) 3999.
[17] Y.S. Su, J.Y. Ying, W.H. Green, Journal of Catalysis 218 (2003) 321.
[18] J. Sun, J.W. Thybaut, G.B. Marin, Catalysis Today 137 (2008) 90.
[19] Y.D. Tong, J.H. Lunsford, Journal of the American Chemical Society 113 (1991) 4741.
[20] Y. Simon, F. Baronnet, P.M. Marquaire, Industrial & Engineering Chemistry Research 46 (2007) 1914.
[21] Z.S. Andrianova, A.N. Ivanova, P.E. Matkovskii, G.P. Startseva, Kinetics and Catalysis 37 (1996) 246.
[22] M. Daneshpayeh, A. Khodadadi, N. Mostoufi, Y. Mortazavi, R. Sotudeh-Gharebagh, A. Talebizadeh, Fuel Processing and Technology 90 (2009) 403.
[23] S. Lacombe, Z. Durjanova, L. Mleczko, C. Mirodatos, Chemical Engineering Technology 18 (1995) 216.
[24] Y. Simon, F. Baronnet, P.M. Marquaire, Industrial and Engineering Chemistry Research 46 (2007) 1914.
[25] M.Y. Sinev, Russian Journal of Physical Chemistry B 1 (2007) 412.
[26] C.T. Tye, A.R. Mohamed, S. Bhatia, Chemical Engineering Journal 87 (2002) 49.
[27] D. Wolf, R. Moros, Chemical Engineering Science 52 (1997) 1189.
[28] L.M. Aparicio, S.A. Rossini, D.G. Sanfilippo, J.E. Rekoske, A.A. Trevino, J.A. Dumesic, Industrial & Engineering Chemistry Research 30 (1991) 2114.
[29] H. Zanthoff, Z. Zhang, T. Grzybek, L. Lehmann, M. Baerns, Catalysis Today 13 (1992) 469.
[30] C. Shi, M. Hatano, J.H. Lunsford, Catalysis Today 13 (1992) 191.
[31] M. Bistolfi, G. Fornasari, M. Molinari, S. Palmery, M. Dente, E. Ranzi, Chemical Engineering Science 47 (1992) 2647.
[32] Q. Chen, J.H.B.J. Hoebink, G.B. Marin, Industrial & Engineering Chemistry Research 30 (1991) 2088.
[33] M.Y. Sinev, Z.T. Fattakhova, V.I. Lomonosov, Y.A. Gordienko, Journal of Natural Gas Chemistry 18 (2009) 273.
[34] O.V. Buyevskaya, M. Rothaemel, H.W. Zanthoff, M. Baerns, Journal of Catalysis 146 (1994) 346.
[35] E.V. Kondratenko, O.V. Buyevskaya, M. Soick, M. Baerns, Catalysis Letters 63 (1999) 153.
[36] M.A. Vannice, Kinetics of Catalytic Reactions, Springer, New York/London, 2005.
[37] S. Lacombe, C. Geantet, C. Mirodatos, Journal of Catalysis 151 (1995) 439.
[38] D. Wolf, M. Slinko, E. Kurkina, Baerns, Applied Catalysis A: General 166 (1998) 47.
[39] P.M. Couwenberg, Q. Chen, G.B. Marin, Industrial & Engineering Chemistry Research 35 (1996) 415.
[40] P.W. Cowenberg, Kinetic studies of methane oxidative coupling, PhD Thesis, Chemical Engineering Department, Einhoven University, Einhoven, 1995.
[41] H.H. Rosenbrock, The Computer Journal 3 (1960) 175.
[42] P.T. Boggs, J.R. Donaldson, R.H. Byrd, R.B. Schnabel, ACM Transactions on Mathematical Software 15 (1989) 348.
[43] K. Huang, X.L. Zhan, F.Q. Chen, D.W. Lu, Chemical Engineering Science 58 (2003) 81.
[44] N. Schumacher, A. Boisen, S. Dahl, A.A. Gokhale, S. Kandoi, L.C. Grabow, J.A. Dumesic, M. Mavrikakis, I. Chorkendorff, Journal of Catalysis 229 (2005) 265.
[45] A. Michaelides, Z.P. Liu, C.J. Zhang, A. Alavi, D.A. King, P. Hu, Journal of the American Chemical Society 125 (2003) 3704.